SCIENTIFIC REPORTS
nature research

Check for updates

OPEN

Facile decoding of quantitative signatures from magnetic nanowire arrays

Mohammad Reza Zamani Kouhpanji[1,2], Ali Ghoreyshi[3], P. B. Visscher[4] & Bethanie J. H. Stadler[1]✉

Magnetic nanoparticles have been proposed as contact-free minimal-background nanobarcodes, and yet it has been difficult to rapidly and reliably decode them in an assembly. Here, high aspect ratio nanoparticles, or magnetic nanowires (MNWs), are characterized using first-order reversal curves (FORC) to investigate quantitative decoding. We have synthesized four types of nanowires (differing in diameter) that might be used for barcoding, and identified four possible "signature" functions that might be used to quickly distinguish them. To test this, we have measured the signatures of several combination samples containing two or four different MNW types, and fit them to linear combinations of the individual type signatures to determine the volume ratios of the types. We find that the signature which determines the ratios most accurately involves only the slope of each FORC at its reversal field, which requires only 2–4 data points per FORC curve, reducing the measurement time by a factor of 10 to 50 compared to measuring the full FORC.

Magnetic nanowires (MNWs) are increasingly impacting biomedical applications[1–6], environmental sciences[7,8], and quantum devices[9–12]. A unique benefit of MNWs is that they can be excited indirectly using an external field, regardless of their surroundings[5,13–15]. Especially in biomedical applications, it is essential to locate, identify, and quantify the targeted MNWs, while using multiple types of MNWs for enriching and multiplexing biological entities[4,15–17].

MNWs have been characterized by measuring their magnetization at various applied fields using hysteresis loops and/or first-order reversal curves (FORC). Accuracy and speed are competing criteria—hysteresis loop measurements are relatively fast but contain significantly less information than FORC measurements, which typically have 50–100 × more measurement points. For example, hysteresis loops measure saturation magnetization and coercivity, which are sufficient to describe a single type of non-interacting MNW[18–21]. However, hysteresis loops cannot fully describe arrays with multiple types of MNWs, especially if there are interactions between the MNWs[22–24]. FORC, on the other hand, can separate the signals of different types of MNWs but the technique is much slower than hysteresis loops. Theoretical models, such as the mean-field model, have been used to quantify the information in FORC diagrams[25,26] by considering perfect arrangements of MNWs with homogeneous properties. These ideal assumptions are not well-satisfied by experimental arrays of MNWs, especially those grown inside polycarbonate templates where the MNW distribution is random.

Historically, FORC measurements have provided qualitative and quantitative descriptions of complex nanomagnetic systems[21,27–29]. Mayergoyz[30,31] proposed the current conventional FORC measurement as an identification technique for the classical Preisach model[32], which describes magnetic hysteresis loops as a superposition of numerous independent switches, called hysterons, with rectangular hysteresis loops, such as those of isolated MNWs acting like Stoner-Wohlfarth particles[33,34]. Experimentally, FORC measurements start with applying a large magnetic field H_{sat}, to ensure the positive saturation of the sample, Fig. 1. The field is then reduced to a predefined field, known as a reversal field, H_r. The moment of the sample is measured while the applied field, H, is slowly increased back to H_{sat}. This process is repeated with different reversal fields H_r to collect a family of magnetization curves, $M(H, H_r)$, as a function of H_r and H. Mathematically, the FORC distribution is defined[31] as

[1]Department of Electrical and Computer Engineering, University of Minnesota Twin Cities, Minneapolis, MN 55455, USA. [2]Department of Biomedical Engineering, University of Minnesota Twin Cities, Minneapolis, MN 55455, USA. [3]Seagate Technology, Bloomington, MN 55435, USA. [4]Department of Physics, University of Alabama, Tuscaloosa, AL 35487-0324, USA. ✉email: stadler@umn.edu

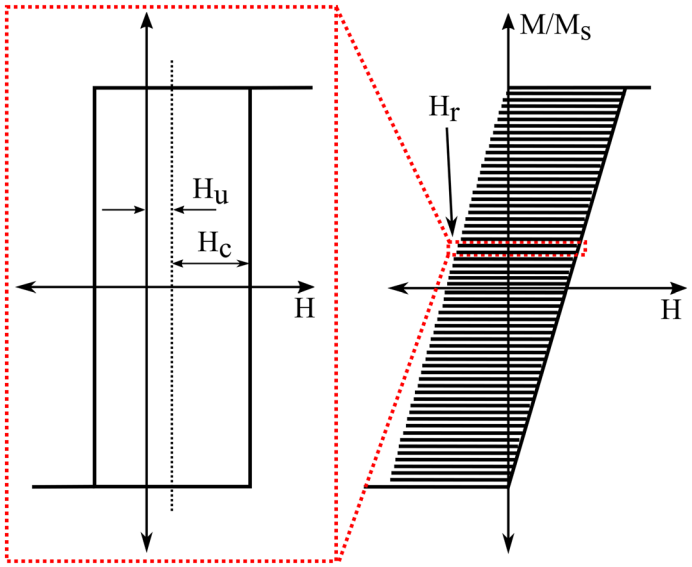

Figure 1. A schematic FORC measurement with interacting hysterons according to the Preisach model. The inset is a schematic of an individual hysteron, which switches down at the reversal field H_r.

$$\rho = -\frac{1}{2}\frac{\partial^2 M(H, H_r)}{\partial H \partial H_r} \tag{1}$$

The FORC results are typically plotted as heat-maps with axes of coercivity, defined by $H_c = (H\text{-}H_r)/2$, and interaction field, defined by $H_u = (H + H_r)/2$, see Figures SI-1 and SI-2.

Although the FORC technique is an exceptional method for the qualitative and sometimes quantitative explanation of complex systems[36–39], it has three main drawbacks. First, FORC usually requires very long measurement times, which is not efficient for biomedical applications or industrial quality control[40–42]. Second, smoothing is required for data processing and can induce spurious features[43–46]. Third, taking two derivatives amplifies noise that can conceal the real features.

It is our objective in this paper to use MNWs as labels or barcodes, which requires that we be able to quickly measure the amounts of each type of MNW in a combined sample. In principle this can be done by fitting the entire FORC distribution to a linear combination of single-type FORC distributions—in fact there is extensive work on this in the rock magnetism literature[27]. In that case, the components are intimately mixed crystallites of different minerals, so that interactions may invalidate the assumption of linear superposition. Our problem is a bit easier in that each type of MNW is not close to the other types in our combinations, so the pure signatures combine linearly. However, determining the entire FORC distribution is time-consuming. For our purpose, we need a signature that can be measured and fit more quickly, and that is ideally a function of one rather than two variables. Two such distributions are often extracted in FORC analysis: the coercivity distribution (P_{Hc}) and interaction field distributions (P_{Hu}). These are projections of the FORC heat-maps onto the H_c and H_u axes[18,24,35] using the integrals:

$$P_{H_c}(H_c) = \int_{-\infty}^{\infty} \rho(H_c, H_u) dH_u \quad \text{and} \quad P_{H_u}(H_u) = \int_{0}^{\infty} \rho(H_c, H_u) dH_c \tag{2}$$

We will use these as two of the four "signatures" for rapid characterization of our MNW systems. The last two are also functions of one variable that can be extracted from a FORC experiment (but can also be measured more rapidly): the projection the FORC heat-map onto the H_r axis, which is mathematically equivalent to the irreversible switching field distribution (ISFD), and the backfield remanence magnetization (BRM), both of which will be defined below.

Experimental methods

As a proof of concept, four types of cobalt (Co) magnetic nanowires (MNWs) with average diameters of 32 nm, 55 nm, 110 nm, and 208 nm were prepared using a well-established template-assisted electrodeposition technique[20,21] (see SI including Figure SI-3). Each of the four MNW types was measured individually with the FORC technique (magnetic field applied parallel to the MNWs axes), Figure SI-1. Next, several combinations were created with at least two different types of MNWs, and the FORC measurements were repeated, Figure SI-2. For quantitative decoding, the individual magnetic signatures were extracted from each combination FORC measurement using four different signatures: (1) the coercivity distribution (P_{Hc}), (2) the interaction field distribution (P_{Hu}), (3) irreversible switching field distribution (ISFD), and (4) the backfield remanence magnetization (BRM).

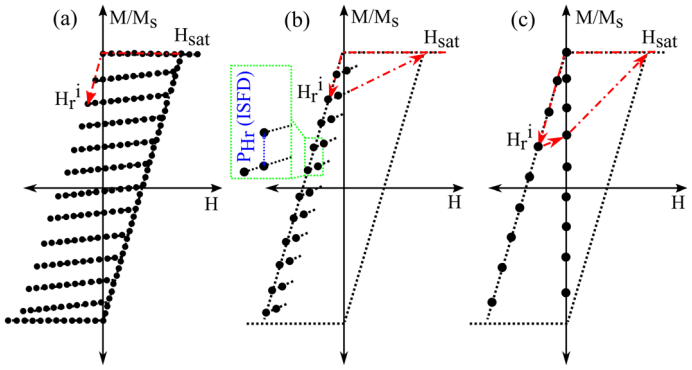

Figure 2. Schematic comparison of conventional FORC and alternative methods with necessary data (black dots). The red dashed lines show the direction of the field change. (**a**) Conventional FORC typically measures ~ 100 data points for each reversal curve, (**b**) ISFD requires only two data points on each reversal curve (as shown), and (**c**) BRM measures magnetization at zero field after the application of each H_r.

The first and second signatures (P_{Hc} and P_{Hu}) are calculated using Eq. (2) which project the FORC heat-maps on the H_c and H_u axes, respectively. The third signature is related to the "switching field distribution" (SFD) which is conventionally defined as the derivative of the upper branch of the hysteresis loop [in our notation, $M(H, H_r)$ at $H = H_r$]:

$$\mathrm{SFD}(H) = \frac{1}{2}\frac{\partial M(H,H)}{\partial H} = \frac{1}{2}\frac{\partial M(H,H_r)}{\partial H_r}\bigg|_{H_r=H} + \frac{1}{2}\frac{\partial M(H,H_r)}{\partial H}\bigg|_{H_r=H} \tag{3}$$

The term "switching field distribution" is slightly unfortunate because elements "switch" at specific fields only in a system of ideal Preisach hysterons—however, the term is well established so we will use it here. Note that the change in M upon switching is twice the saturation moment—if we define SFD to be the amount of saturation moment switching per unit field, we get the factor of 1/2 shown in Eq. (3). The first term in Eq. (3) vanishes for a reversible system, so we will refer to it as the irreversible SFD (ISFD), and the second term as the reversible SFD. It is schematically shown as the blue line in Fig. 2b. Mathematically, ISFD is also proportional to the projection of the FORC heat-maps onto the H_r axis by integrating over all applied fields:

$$\int_{H_r}^{\infty} \rho(H,H_r)dH = -\frac{1}{2}\frac{\partial M(H,H_r)}{\partial H_r}\bigg|_{H=\infty} + \frac{1}{2}\frac{\partial M(H,H_r)}{\partial H_r}\bigg|_{H=H_r} = 0 + \frac{1}{2}\frac{\partial M(H,H_r)}{\partial H_r}\bigg|_{H=H_r} \tag{4}$$

Note that the first term is zero because the magnetization does not change with H_r at large values of applied field (H) due to saturation.

Finally, the fourth signature (BRM) is the value of magnetization of the sample when the applied field is brought to zero after each application of different H_r values, Fig. 2c.

To determine which of these four magnetic signatures reliably and quantitatively decodes the amounts and types of the MNW in the combinations, we fit the signature of the combination to a linear superposition of the magnetic signatures from individual MNWs types ("volumetric fit" in the figures). For example, for the P_{Hc} signature of a combination of MNWs with diameters of 55 nm and 208 nm,

$$\textit{Volumetric fit for } P_{Hc} = \alpha_{55\,\mathrm{nm}} P_{Hc55\,\mathrm{nm}} + \alpha_{208\,\mathrm{nm}} P_{Hc208\,\mathrm{nm}} \tag{5}$$

where the volume fraction $\alpha_{55\mathrm{nm}}$ = (volume of Co in 55 nm wires)/(total volume of Co) and similarly for $\alpha_{208\,\mathrm{nm}}$, so that $\alpha_{55\,\mathrm{nm}} + \alpha_{208\,\mathrm{nm}} = 1$. The RMS error is defined as

$$RMS = \sqrt{\frac{1}{N}\sum_{i=1}^{N}\left(Exp.data - Volumetric\,fit\right)^2} \tag{6}$$

where N is the number of data-points for the corresponding signature. The α_i coefficients are found by minimizing the RMS. The volume ratio (x) is then

$$x = \frac{\alpha_{208\,\mathrm{nm}}}{\alpha_{55\,\mathrm{nm}}} \tag{7}$$

Each magnetic signature is explained in detail below, and then we explain how the minimum number of points shown in Fig. 2b can be used to obtain the best quantitative signatures with orders of magnitude fewer data points than conventional FORC.

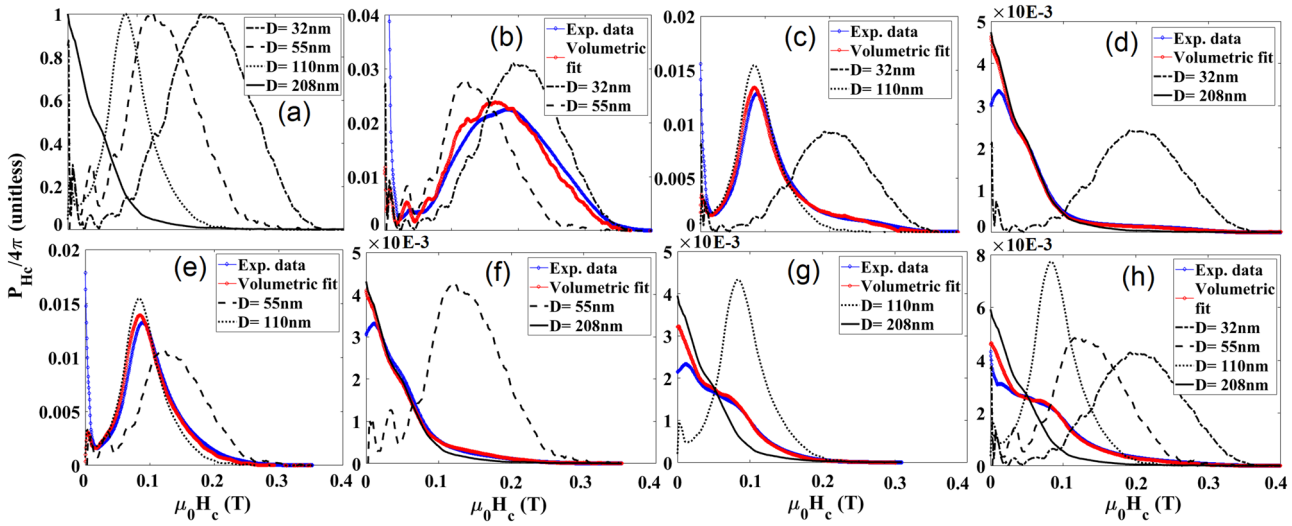

Figure 3. Coercivity distribution (P_{Hc}, determined by taking an integral over H_u from FORC heat-maps) for (**a**) normalized for individual types of MNWs, (**b**–**g**) different combinations of two types of MNWs, as indicated in the legend and (**h**) one combination of four types. The blue lines show measurements of combinations, and the red lines show the best match for combinations of the individual signatures (from **a**) using volume ratio, see Table 1.

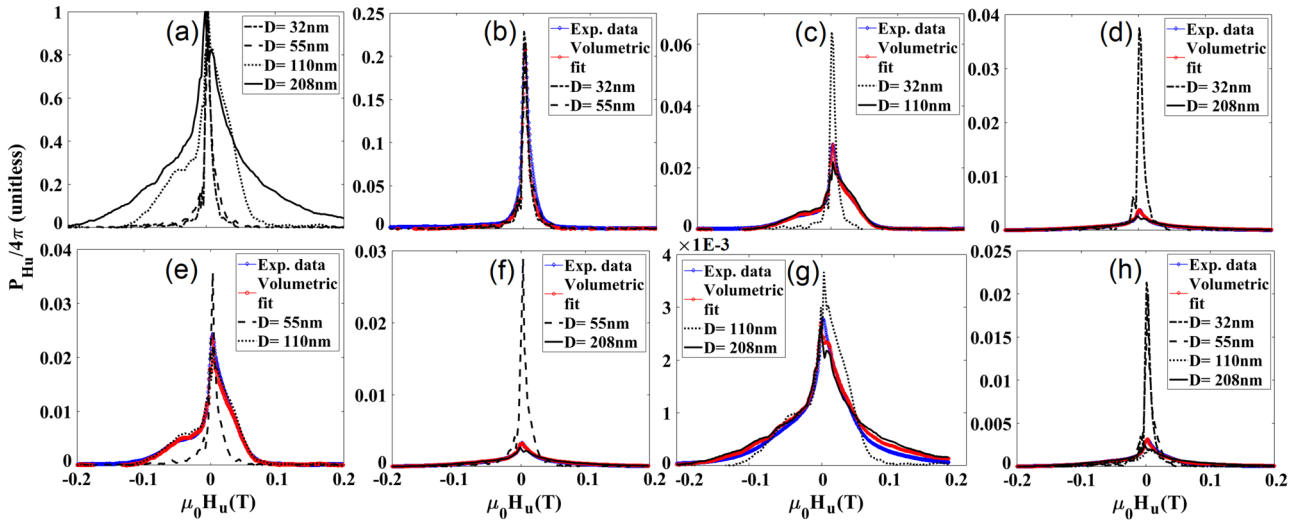

Figure 4. Interaction distribution (P_{Hu}, the integral over H_c from the FORC heat-maps) for (**a**) normalized for individual types of MNWs, (**b**–**g**) different combinations of two types of MNWs, as indicated in the legend and (**h**) one combination of four types . The blue lines show measurements of combinations, and the red lines show the best match for combinations of the individual signatures (from **a**) using volume ratio, see Table 1.

Results

The FORC data and heat-maps were measured and processed using the conventional FORC protocols to obtain signatures for the four Co MNWs samples that contained a single type of MNW (32 nm, 55 nm, 110 nm, and 208 nm), Figure SI-1. Similar conventional FORC measurements and processing were performed for all six combinations of two MNW types and for one combination that included all four MNW types, Figure SI-2.

For quantitative decoding, the FORC heat-maps were first projected on the H_c and H_u axes to find the coercivity distribution (P_{Hc}) and interaction distribution (P_{Hu}), respectively. The P_{Hc} and P_{Hu} signatures of individual types of nanowires are shown in parts (a) of Figs. 3 and 4. Combinations of these individual types were then measured (blue lines) and the volume fractions α_i were chosen to minimize the RMS error (Eq. 6). Table 1 gives the resulting relative volume fractions.

Of our first two signatures, the projections onto the H_u and H_c axes, P_{Hu} is the more effective signature for most combinations with the largest error being 50% overestimation of 208 nm MNWs in a combination with 55 nm MNWs. This may seem like a large error, but many multiplexed nanoparticle diagnoses to date use log scales to plot populations due to large potential offsets[5]. For example, fluorescence labels have large errors due to background lighting and bleaching[4]. While this is the case, here we are interested in finding the best magnetic

	1:x	x from P_{Hc}		x from P_{Hu}		x from ISFD		x from BRM	
	Known x	Fit	Error	Fit	Error	Fit	Error	Fit	Error
Combinations of two									
32 nm:55 nm	1.1	0.38	−0.63	2.6	1.5	0.70	−0.33	0.47	−0.56
32 nm:110 nm	5.8	42	6.3	5.1	−0.11	2.6	−0.54	21	2.7
32 nm:208 nm	23	880	37	23	−0.01	20	−0.13	120	4.0
55 nm:110 nm	5.5	27	3.8	4.5	−0.18	2.3	−0.58	12	1.2
55 nm:208 nm	22	440	19	34	0.52	20	−0.09	98	3.4
110 nm:208 nm	4.0	11	1.8	14	2.5	3.4	−0.15	3.5	−0.14
Combination of four									
32 nm	1	1	0	0	–	1	0	1	0
55 nm	1.1	0.95	−0.14	0.091	−0.92	1.2	0.12	0.27	−0.75
110 nm	5.8	26	3.4	0.73	−0.87	2.8	−0.52	4.2	−0.27
208 nm	23	270	11	16	−0.30	16	−0.32	11	−0.53

Table 1. Comparison of extracted volume ratios. The ratio x is normalized to the first type listed, i.e., in the first row $x = \alpha_{55\ nm}/\alpha_{32\ nm}$.

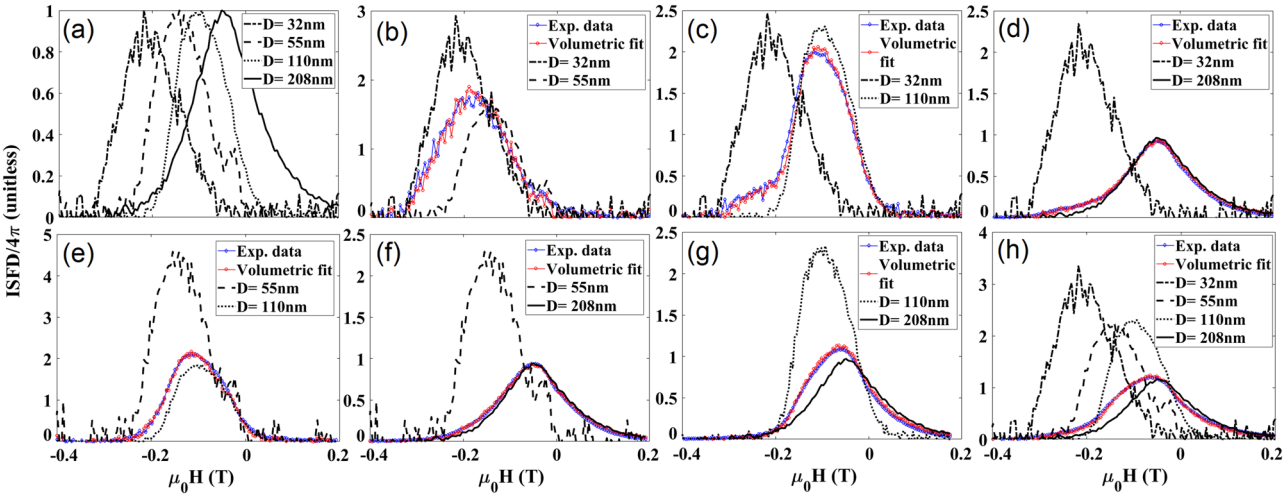

Figure 5. Irreversible switching field distribution (ISFD) results, (**a**) normalized for individual types of MNWs, (**b**–**g**) different combinations of two types of MNWs, as indicated in the legend and (**h**) one combination of four types. The blue circles show measurements of combinations, and the red circles show the best match for combinations of the individual signatures (from **a**) using volume ratio, see Table 1.

signature for decoding MNWs, so that these signatures are known for comparisons to other labelling systems in future studies.

The first two signatures P_{Hu} and P_{Hc} require taking two derivatives of the FORC data followed by an integral, but this can be avoided by using the irreversible switching field distribution (ISFD) or backfield remanence magnetization (BRM). Both ISFD and BRM can be obtained directly from the raw data (see Fig. 2). Specifically, ISFD is the change in magnetization at the same applied field when we change the reversal field, Fig. 2b. BRM is the magnetization at zero applied field after applying and removing each H_r, Fig. 2c.

ISFD as a signature can be characterized by two parameters: (I) the amplitude of the local peak associated with each MNW type, proportional to the volume fraction of that type), and (II) the relative location of the peaks (dominated by the coercivity of the MNW type), Fig. 5a. For combined samples, ISFD broadens and forms two local peaks associated with the coercivities of the individual MNWs in each combination where the heights of the peaks indicate the amount of each MNW relative to another.

It should be emphasized that the sensitivity of ISFD depends on both of the amount, the fraction of irreversible switching, and coercivity of component MNWs, with the latter being the dominant parameter. Therefore, combinations of MNWs can be designed for optimal quantitative decoding by combining high coercivity and low coercivity "signatures"[15]. For example, in Fig. 5d, the combination contains 22 × more volume of 208 nm-diameter MNWs than 32 nm-diameter MNWs. However, this ratio was easily quantified with high accuracy due to separated peaks in ISFD, third column parameter in Table 1. Combinations of 32 nm or 55 nm MNWs with 110 nm MNWs had the most error (~ 50%) due to the combination of large volume ratios (~ 1:5) and the similarities in coercivity. When the volume ratio was closer (1:1 or 1:4), the coercivities of MNW "barcodes" could

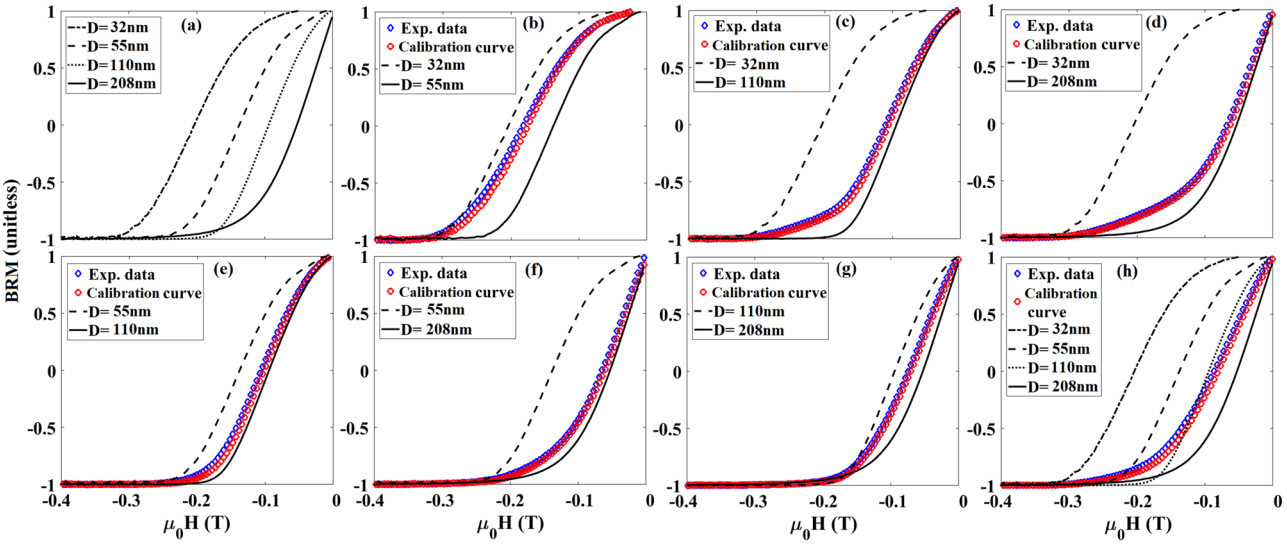

Figure 6. Normalized backfield remanence magnetization (BRM) results for (**a**) individual types of MNW, (**b**–**g**) different combinations of two types of MNWs, as indicated in the legend and (**h**) one combination of four types. The blue circles show measurements of combinations, and the red circles show the best match for combinations of the individual signatures (from **a**) using volume ratio, see Table 1.

be closer without as much impact on decoding the combination. This technique also yielded the best results for decoding all four Co MNW codes from the single 4-way combination, lower section of Table 1.

BRM curves for single MNW types and combinations are shown in Fig. 6. Since the combinations had different magnetic moments, we normalized BRM with respect to their saturation backfield remanence (remanence of the major hysteresis loop, M_{sbr}) to render them from − 1 to + 1. From Fig. 6, it can be seen that the BRM value of any combination is always between the BRM values of the individual MNWs in the combination. Therefore, the BRM shift in the combinations determines the amounts of each MNW present. Two features characterize BRM as a signature[47–50]: (I) the field where it is zero, which is average coercivity of the MNWs, and (II) its overall slope which is correlated to the interaction fields. The fourth parameter in Table 1 has the results of volume ratio calculations. Although this measurement can be very fast compared to P_{Hc} and P_{Hu}, ISFD appears to be the best signature for these Co MNWs.

As mentioned in the Experimental Method section, the volume ratio of MNWs present in each combination was calculated using a weighted sum of the individual signatures (parts (a) of the preceding figures) where RMS error between each calculated curve and its respective measured combination curve was minimized. The ratios of these weights, which are the volume of each MNW type, determine to the volume ratios of the MNWs present in each combination. For each of the four magnetic signatures (P_{Hc}, P_{Hu}, ISFD, and BRM), these volume ratios were tabulated with the known volume ratio for comparison in Table 1. Italic emphasis highlighting was used to show which MNW combinations-signature pairs measured the volume ratio within a factor of 2 (corresponding to + /− 100% error). Most commonly used nanobarcodes, especially in the nanomedicine or biology, use optical nanobarcodes such as fluorescent dyes or quantum dots nanoparticles[4,5,13,15,51]. These barcode methods typically plot calculated values and errors on log scales, where a factor of 2 is quite small. In this regard, ISFD appears to be an excellent signature for overall decoding MNW combinations. The most effective multiplexing systems, however, will use a combination of techniques. For example, fluorescently-labelled magnetic nanowires could be detected by independent optical and magnetic techniques. Here, we simply report a promising magnetic technique, which has great potential to help future studies of many kinds.

As alluded to above, both ISFD and BRM can also be measured much more quickly than conventional FORC, and involve much simpler and faster data processing. This makes ISFD even more ideal for real-time diagnosis and quality control. Specifically, these signatures do not require massive data processing as required by the conventional FORC analysis[43–46]. For example, conventional FORC analysis typically requires 20–100 curves with 20–100 points each (= 400 to 10,000 points). In contrast, Figs. 2b and 7 show how the ISFD can be calculated from substantially fewer points on each magnetization curve (= 40–200 points). The results in Fig. 5 were calculated using only two points—to test the effect of smoothing, we repeated the analysis using 4 points (as shown in Fig. 7) and similarly with 6 points. The results are given in Figures SI-5 and SI-6, and there was not a notable deviation in ISFD.

Also, BRM only requires the magnetization at one point, namely zero-field (H = 0) after applying each reversal field (= 20–100 points). It should be emphasized that the BRM measurement is slightly different from the standard remanence measurements, such as isothermal remanence or DC demagnetization remanence, for example[50,52–55]. The BRM protocol saturates combinations before applying and removing each reversal field while the standard remanence protocols measure the remanence after applying and removing a continuous ascending or descending field. Although this signature was not highly effective for the Co MNWs in this study,

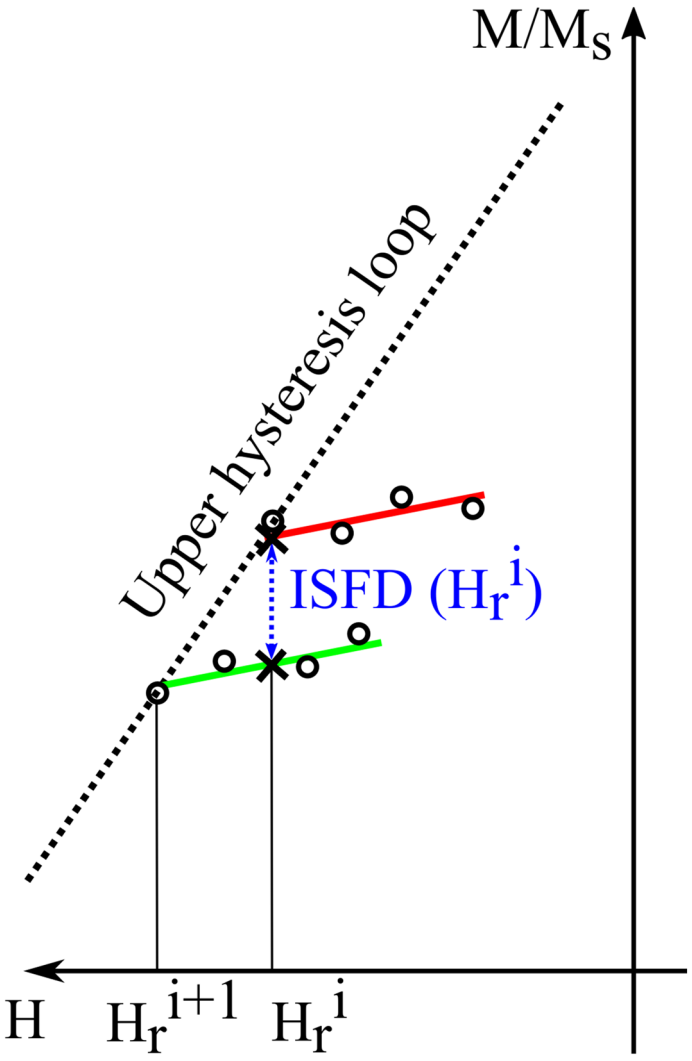

Figure 7. Calculation of smoothed ISFD: The upper (red) FORC begins at H_r^i and has four measured points (black dots). A straight red line is least-squares fit to these points. The lower FORC begins at H_r^{i+1} and its points are similarly fit to the green line. The black Xs are the points on the two lines with $H = H_r^i$, and the vertical distance between them is proportional to the ISFD.

future magnetic nanoparticles could be engineered to have large BRM differentiation to take advantage of this potentially fast decoding method.

Conclusions

Irreversible switching field distribution (ISFD) was identified as an overall promising signature for decoding MNWs. Both ISFD and BRM can be determined 10–50 × faster than conventional FORC signatures with much simpler data processing. Regardless of the type of MNW, measurement instrument, and the data acquisition system, ISFD and BRM are fast because they require substantially fewer data points. In summary, ISFD has great potential to accelerate decoding, enabling new industry-friendly quality control and real-time diagnosis.

Data availability

The datasets collected and/or analyzed during the current study are available from the corresponding author on a reasonable request.

Received: 23 October 2019; Accepted: 27 July 2020
Published online: 23 September 2020

References

1. Jeon, Y. S. *et al.* Metallic Fe–Au barcode nanowires as a simultaneous T cell capturing and cytokine sensing platform for immunoassay at the single-cell level. *ACS Appl. Mater. Interfaces* **11**, 23901–23908 (2019).

2. Martínez-Banderas, A. I. *et al.* Iron-based core–shell nanowires for combinatorial drug delivery and photothermal and magnetic therapy. *ACS Appl. Mater. Interfaces* **11**, 43976–43988 (2019).
3. Safronov, A. P. *et al.* Polyacrylamide ferrogels with Ni nanowires. *Materials (Basel)* **12**, 2582 (2019).
4. Zamani Kouhpanji, M. R., Um, J. & Stadler, B. J. H. Demultiplexing of magnetic nanowires with overlapping signatures for tagged biological species. *ACS Appl. Nano Mater.* **3**, 3080–3087 (2020).
5. Zamani Kouhpanji, M. R. & Stadler, B. J. H. A guideline for effectively synthesizing and characterizing magnetic nanoparticles for advancing nanobiotechnology: A review. *Sensors* **20**, 2554 (2020).
6. Nemati, Z. *et al.* Magnetic isolation of cancer-derived exosomes using Fe/Au magnetic nanowires. *ACS Appl. Nano Mater.* **3**, 2058–2069 (2020).
7. Moreno, J. A. *et al.* Growth of ordered iron oxide nanowires for photo-electrochemical water oxidation. *ACS Appl. Energy Mater.* **2**, 8473–8480a (2019).
8. Cui, H., Shi, J., Yuan, B. & Fu, M. Synthesis of porous magnetic ferrite nanowires containing Mn and their application in water treatment. *J. Mater. Chem. A* **1**, 5902–5907. https://doi.org/10.1039/c3ta01692g (2013).
9. Mohammed, H. *et al.* Controlled spin-torque driven domain wall motion using staggered magnetic wires. *Appl. Phys. Lett.* **116**, 032402 (2020).
10. Maqableh, M. M. *et al.* Low-resistivity 10 nm diameter magnetic sensors. *Nano Lett.* **12**, 4102–4109 (2012).
11. Parkin, S. & Yang, S.-H. Memory on the racetrack. *Nat. Nanotechnol.* **10**, 195–198 (2015).
12. Um, J. *et al.* Fabrication of long-range ordered aluminum oxide and Fe/Au multilayered nanowires for 3D magnetic memory. *IEEE Trans. Magn.* **56**, 1–6 (2020).
13. Bhana, S., Wang, Y. & Huang, X. Nanotechnology for enrichment and detection of circulating tumor cells. *Micro Nanosyst.* **7**, 1973–1990 (2015).
14. Jeon, I. T. *et al.* Magnetic NiFe/Au barcode nanowires with self-powered motion. *J. Appl. Phys.* **111**, 5–8 (2012).
15. Zamani Kouhpanji, M. R. & Stadler, B. J. H. Projection method as a probe for multiplexing/demultiplexing of magnetically enriched biological tissues. *RSC Adv.* **10**, 13286–13292 (2020).
16. Cho, J. U. *et al.* Effect of field deposition and pore size on Co/Cu barcode nanowires by electrodeposition. *J. Magn. Magn. Mater.* **310**, 2420–2422 (2007).
17. Lee, J. H. *et al.* Iron-gold barcode nanowires. *Angew. Chem. Int. Ed.* https://doi.org/10.1002/anie.200605136 (2007).
18. Zamani Kouhpanji, M. R. & Stadler, B. J. H. Beyond the qualitative description of complex magnetic nanoparticle arrays using FORC measurement. *Nano Express* **1**, 010017 (2020).
19. Kouhpanji, M. R. Z. & Stadler, B. J. H. Assessing the reliability and validity ranges of magnetic characterization methods. *ArXiv* 1–9 (2020).
20. Kouhpanji, M. R. Z., Visscher, P. B. & Stadler, B. J. H. Underlying magnetization responses of magnetic nanoparticles in assemblies. *arXiv* **1**, 1–7 (2020).
21. Kouhpanji, M. R. Z. & Stadler, B. J. H. Quantitative description of complex magnetic nanoparticle arrays. arXiv:1911.12480 1–9 (2019).
22. Palmero, E. M. *et al.* Stepwise magnetization reversal of geometrically tuned in diameter Ni and FeCo bi-segmented nanowire arrays. *Nano Res.* **12**, 1547–1553 (2019).
23. Fernández, J. G., Martínez, V. V., Thomas, A., de la Prida Pidal, V. M. & Nielsch, K. Two-step magnetization reversal FORC fingerprint of coupled bi-segmented Ni/Co magnetic nanowire arrays. *Nanomaterials* **8**, 1–15 (2018).
24. Ramazani, A., Asgari, V., Montazer, A. H. & Kashi, M. A. Tuning magnetic fingerprints of FeNi nanowire arrays by varying length and diameter. *Curr. Appl. Phys.* **15**, 819–828 (2015).
25. Gilbert, D. A. *et al.* Quantitative decoding of interactions in tunable nanomagnet arrays using first order reversal curves. *Sci. Rep.* **4**, 1–5 (2014).
26. Dobrotă, C.-I. & Stancu, A. Tracking the individual magnetic wires' switchings in ferromagnetic nanowire arrays using the first-order reversal curves (FORC) diagram method. *Phys. B Condens. Matter* **457**, 280–286 (2015).
27. Carvallo, C., Muxworthy, A. R. & Dunlop, D. J. First-order reversal curve (FORC) diagrams of magnetic mixtures: Micromagnetic models and measurements. *Phys. Earth Planet. Inter.* **154**, 308–322 (2006).
28. Roberts, A. P., Heslop, D., Zhao, X. & Pike, C. R. Understanding fine magnetic particle systems through use of first-order reversal curve diagrams. *Rev. Geophys.* **52**, 557–602 (2014).
29. Dobrotă, C.-I. & Stancu, A. What does a first-order reversal curve diagram really mean? A study case: Array of ferromagnetic nanowires. *J. Appl. Phys.* **113**, 043928 (2013).
30. Mayergoyz, I. D. Mathematical models of hysteresis (invited). *IEEE Trans. Magn.* **22**, 603–608 (1986).
31. Mayergoyz, I. D. The classical Preisach model of hysteresis and reversibility. *J. Appl. Phys.* **69**, 4602–4604 (1991).
32. Preisach, F. Uber die magnetische nachwirkung. *Mitteilung aus dem Zentrallaboratorium des Wernerwerkes der Siemens Halske* **277**, 277–302 (1935).
33. Stancu, A., Pike, C., Stoleriu, L., Postolache, P. & Cimpoesu, D. Micromagnetic and preisach analysis of the first order reversal curves (FORC) diagram. *J. Appl. Phys.* **93**, 6620–6622 (2003).
34. Dobrotă, C. I. & Stancu, A. What does a first-order reversal curve diagram really mean? A study case: Array of ferromagnetic nanowires. *J. Appl. Phys.* **113**, 043928 (2013).
35. Valcu, B. F., Gilbert, D. A., Liu, K. & Technology, S. Fingerprinting inhomogeneities in recording media using the first-order reversal curve method. *IEEE Trans. Magn.* **47**, 2988–2991 (2011).
36. Pike, C. R., Roberts, A. P. & Verosub, K. L. Characterizing interactions in fine magnetic particle systems using first order reversal curves. *J. Appl. Phys.* **85**, 6660–6667 (1999).
37. Frampton, M. K. *et al.* First-order reversal curve of the magnetostructural phase transition in FeTe. *Phys. Rev. B* **214402**, 1–8 (2017).
38. Gilbert, D. A. *et al.* Probing the A 1 to L 10 transformation in FeCuPt using the first order reversal curve method. *APL Mater.* **2**, 086106 (2014).
39. Ruta, S. *et al.* First order reversal curves and intrinsic parameter determination for magnetic materials; Limitations of hysteron-based approaches in correlated systems. *Sci. Rep.* **7**, 1–12 (2017).
40. Gräfe, J., Schmidt, M., Audehm, P., Schütz, G. & Goering, E. Application of magneto-optical Kerr effect to first-order reversal curve measurements. *Rev. Sci. Instrum.* **85**, 023901 (2014).
41. De Biasi, E. Faster modified protocol for first order reversal curve measurements. *J. Magn. Magn. Mater.* **439**, 259–268 (2017).
42. Rivas, M., Gorria, P., Muñoz-Gómez, C. & Martińez-García, J. C. Quasi-static AC FORC measurements for soft magnetic materials and their differential interpretation. *IEEE Trans. Magn.* **53**, 2–7 (2017).
43. Harrison, R. J. & Feinberg, J. M. FORCinel: An improved algorithm for calculating first-order reversal curve distributions using locally weighted regression smoothing. *Geochem. Geophys. Geosyst.* **9**, 1–11 (2008).
44. Cimpoesu, D., Dumitru, I. & Stancu, A. DoFORC tool for calculating first-order reversal curve diagrams of noisy scattered data. *J. Appl. Phys.* **125**, 023906 (2019).
45. Groß, F. *et al.* gFORC: A graphics processing unit accelerated first-order reversal-curve calculator. *J. Appl. Phys.* **126**, 163901 (2019).
46. Berndt, T. A. & Chang, L. Waiting for forcot: Accelerating FORC processing 100× using a fast-Fourier-transform algorithm. *Geochem. Geophys. Geosyst.* **20**, 6223–6233 (2019).

47. Martnez Huerta, J. M., De La Torre Medina, J., Piraux, L. & Encinas, A. Self consistent measurement and removal of the dipolar interaction field in magnetic particle assemblies and the determination of their intrinsic switching field distribution. *J. Appl. Phys.* **111**, 083914 (2012).
48. Araujo, E., Martínez-Huerta, J. M., Piraux, L. & Encinas, A. Quantification of the interaction field in arrays of magnetic nanowires from the remanence curves. *J. Supercond. Nov. Magn.* **31**, 3981–3987 (2018).
49. Robertson, D. J. & France, D. E. Discrimination of remanence-carrying minerals in mixtures, using isothermal remanent magnetisation acquisition curves. *Phys. Earth Planet. Inter.* **82**, 223–234 (1994).
50. Heslop, D. & Dillon, M. Unmixing magnetic remanence curves without a priori knowledge. *Geophys. J. Int.* **170**, 556–566 (2007).
51. DaCosta, M. V., Doughan, S., Han, Y. & Krull, U. J. Lanthanide upconversion nanoparticles and applications in bioassays and bioimaging: A review. *Anal. Chim. Acta* **832**, 1–33 (2014).
52. De Toro, J. A. *et al.* Remanence plots as a probe of spin disorder in magnetic nanoparticles. *Chem. Mater.* **29**, 8258–8268 (2017).
53. Pfeiffer, H. Determination of anisotropy field distribution in particle assemblies taking into account thermal fluctuations. *Phys. Status Solidi* **118**, 295–306 (1990).
54. Tsoi, G. & Wenger, L. Investigation of magnetic interactions in large arrays of magnetic nanowires. *J. Appl. Phys.* https://doi.org/10.1063/1.2834242 (2014).
55. Elbaile, L., Crespo, R. D., Vega, V. & García, J. A. Magnetostatic interaction in Fe–Co nanowires. *J. Nanomater.* **2012**, 1–6 (2012).

Acknowledgements

This work is based upon work supported primarily by the National Science Foundation under Grant No. CMMI-1762884. Portions of this work were conducted in the Minnesota Nano Center, which is supported by the National Science Foundation through the National Nano Coordinated Infrastructure Network (NNCI) under Award Number ECCS-1542202. Part of this work was performed at the Institute for Rock Magnetism (IRM) at the University of Minnesota. The IRM is a US National Multi-user Facility supported through the Instrumentation and Facilities program of the National Science Foundation, Earth Sciences Division (NSF/EAR 1642268), and by funding from the University of Minnesota.

Author contributions

M.R.Z.K. and B.J.H.S. initiated the original idea and designed the experiments. M.R.Z.K. conducted the samples fabrication, measurements, and processed/analyzed the data. M.R.Z.K., A.G., P.B.V., and B.J.H.S. interpreted the data and contributed to writing/revising the manuscript. B.J.H.S. supervised the study and provided the funding.

Competing interests

The authors declare no competing interests.

Additional information

Supplementary information is available for this paper at https://doi.org/10.1038/s41598-020-72094-4.

Correspondence and requests for materials should be addressed to B.J.H.S.

Reprints and permissions information is available at www.nature.com/reprints.

Publisher's note Springer Nature remains neutral with regard to jurisdictional claims in published maps and institutional affiliations.